AGU100 ADVANCING EARTH AND SPACE SCIENCE

Geophysical Research Letters

RESEARCH LETTER

10.1029/2018GL079349

Rupture in the 4 May 2018 M_W 6.9 Earthquake Seaward of the Kilauea East Rift Zone Fissure Eruption in Hawaii

Chengli Liu[1], **Thorne Lay**[2], **and Xiong Xiong**[1]

[1]Hubei Subsurface Multi-Scale Imaging Key Laboratory, Institute of Geophysics and Geomatics, China University of Geosciences, Wuhan, China, [2]Department of Earth and Planetary Sciences, University of California, Santa Cruz, CA, USA

Abstract The 4 May 2018, M_W 6.9 thrust-faulting earthquake occurred a day after the first fissure eruption in Leilani Estates along the East Rift Zone of Kilauea, Hawaii, relatively early in the 2018 eruptive sequence. The earthquake's location and geodetic deformation pattern are similar to those of the larger 1975 Kalapana earthquake (M_W 7.7), which is thought to have occurred on the décollement between the island volcanics and the former Pacific seafloor. The 2018 event has a shallow-dipping thrust plane and shallow epicenter located just offshore. A finite-fault kinematic slip model is determined by inversion of teleseismic body waves, strong-ground motion recordings, and coseismic Global Positioning System offsets along the southeastern coast of Hawaii. Inversions indicate a preferred dip of 7°, slip of up to 3.0 m near 5-km deep offshore of the coast, and low average rupture speed of ~1 km/s. These are consistent with rupture of a weak décollement.

Plain Language Summary Early in the 2018 eruption sequence at Kilauea volcano in Hawaii, a magnitude 6.9 earthquake occurred just off the coast along the Leilani Estates which had begun to experience fissure eruptions a day earlier. The earthquake was well recorded by global seismic stations and by strong motion instruments on Hawaii, and Global Positioning System offsets during the earthquake were determined along the coastal area. These data are used to determine a space-time history of the earthquake rupture. The slip is concentrated in a band offshore parallel to the coast, and the fault that ruptured is likely to be the boundary between the volcanic pile of the island and the former Pacific Ocean seafloor. As much as 3 m of slip occurred, with the rupture having behavior similar to slow rupturing tsunami earthquakes in subduction zones, indicating a relatively weak fault.

Key Points:
- Teleseismic, strong-motion, and GPS displacement data are inverted to determine the spatiotemporal earthquake slip distribution
- Peak slip is ~3.0 m, average rise time is 4.7 s, rupture speed is 0.7 to 1.6 km/s, and duration is 30 s, indicating low fault strength
- The earthquake likely ruptured the offshore shallow-dipping décollement between the island volcanics and the former Pacific seafloor

Supporting Information:
- Supporting Information S1

Correspondence to:
T. Lay,
tlay@ucsc.edu

Citation:
Liu, C., Lay, T., & Xiong, X. (2018). Rupture in the 4 May 2018 M_W 6.9 earthquake seaward of the Kilauea East Rift Zone fissure eruption in Hawaii. *Geophysical Research Letters*, *45*, 9508–9515. https://doi.org/10.1029/2018GL079349

Received 23 JUN 2018
Accepted 25 AUG 2018
Accepted article online 4 SEP 2018
Published online 19 SEP 2018

1. Introduction

The 2018 eruptive sequence at Kilauea volcano on Hawaii commenced on 17 April 2018 with pressure increase in Pu'u 'O'o, followed by crater collapse on 30 April and drainage of the summit lava lake on 2 May. On 1 May seismicity began migrating to the northeast along the East Rift Zone, the first fissure erupted in Leilani Estates on 3 May, and on 4 May the largest earthquake in the sequence occurred near the coast (22:32:54 UTC, 19.313°N, 154.998°W; U.S. Geological Survey, https://earthquake.usgs.gov/earthquakes/eventpage/us1000dyad#executive). This large earthquake has long-period seismic wave focal mechanisms with shallow-dipping thrust faulting solutions dipping 20° toward the northwest with seismic moment $M_0 = 2.7 \times 10^{19}$ Nm (M_W 6.9). (USGS W-phase solution: https://earthquake.usgs.gov/earthquakes/eventpage/us1000dyad#moment-tensor; and Global Centroid Moment Tensor (GCMT): http://www.globalcmt.org/CMTsearch.html; Ekström et al., 2012). The USGS hypocentral depth is 2.1 ± 3.6 km; centroid depth and dip are likely poorly resolved in long-period moment-tensor solutions for such a shallow source.

The East Rift Zone experienced prior large fissure eruptions in 1955, 1960, 1969, and 1972, along with many smaller eruptions, so it was recognized to be a very active region. Previous large earthquakes struck the East Rift Zone on 29 November 1975 (M_W 7.7) and 26 June 1989 (M_W 6.4), with the 1975 Kalapana epicenter being very close to that of the 2018 event, while the 1989 hypocenter is a few kilometers inland (Figure 1). The Kalapana earthquake has been extensively studied, as it produced coastal subsidence and a damaging tsunami with a maximum height of 14.6 m above the postsubmergence shoreline east of Halape. The focal mechanism of the Kalapana earthquake has a very shallow dip (e.g., Ando, 1979; Crosson & Endo, 1982; Eissler & Kanamori, 1987; Furumoto & Kovach, 1979; Kawakatsu, 1989; Ma et al., 1999; Nettles & Ekström, 2004; Wyss & Kovach, 1988). This event, similar to the great 1868 rupture (Wyss, 1988), is generally interpreted as primarily involving thrust faulting on the shallow ~2° to 5° dipping basal décollement (e.g., Broyles et al., 1979; Morgan et al., 2000; Park et al., 2007) between the island volcanics and the former Pacific sea floor. The

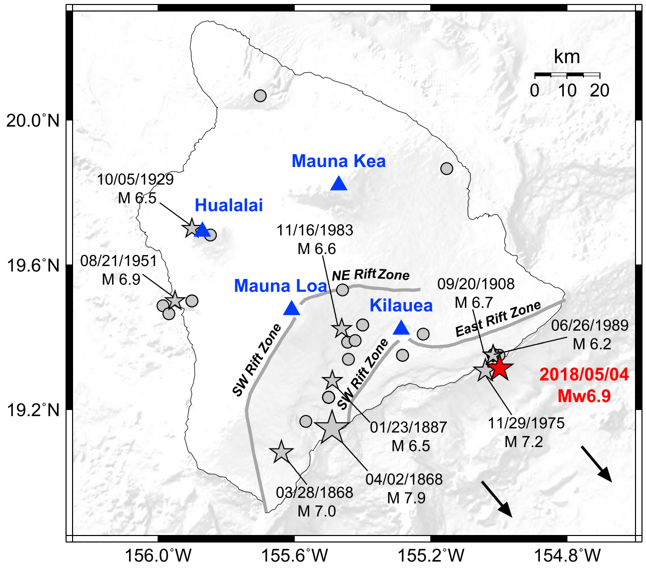

Figure 1. Location map for the 4 May 2018 Hawaii earthquake. The red star indicates the 2018 mainshock epicenter. The dark gray dots locate large historic crustal earthquakes with magnitude less than 6.5, and the gray stars represent the large historic crustal earthquakes with magnitude larger than 6.5 (note the proximity of the 20 September 1908, the 29 November 1975 Kalapana, 1989 and 2018 earthquake epicenters), and the gray thick lines indicate active rift zones. Blue triangles indicate the location of primary volcanoes. The sketch arrows show the direction of relative motion of the mobile southeastern flank of Kilauea.

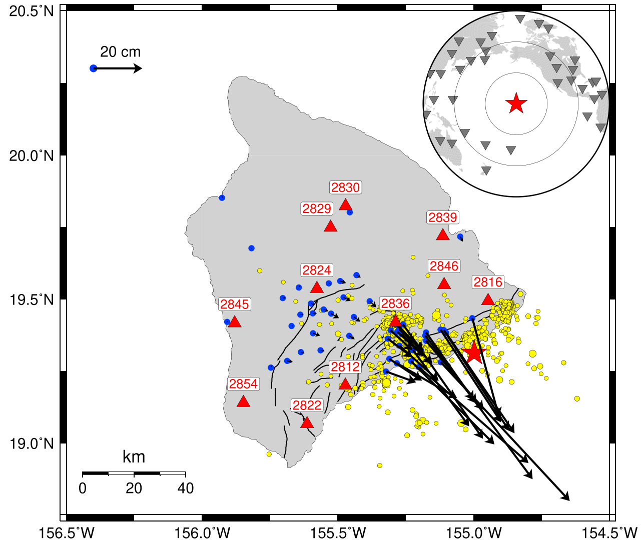

Figure 2. Map view of the near-field seismic and geodetic data coverage. The red star denotes the epicenter of the mainshock. Red triangles indicate locations of strong-motion stations used in the joint inversions. Blue dots and black arrows indicate GPS station locations and coseismic horizontal displacements. The upper right inset panel shows the distribution of teleseismic stations used in the inversion. The black curves represent active faults. Seismicity after the mainshock with magnitude ≥2.5 from 4 May 2018 to 5 June 2018 is shown by the yellow circles.

south flank of Kilauea displaces seaward due to a combination of magma injection in the rift zones and topographic load of the island driving spreading (e.g., Denlinger & Okubo, 1995; Gillard et al., 1996; Morgan et al., 2000; Swanson et al., 1976; Thurber & Gripp, 1988). There was additional near-surface coseismic slumping during the 1975 event, complicating the interpretation of the source (e.g., Day et al., 2005; Eissler & Kanamori, 1987; Ma et al., 1999), but the event was not concurrent with dike injection as in the case of the 2018 event. The 1989 rupture is also a shallowly-dipping (GCMT dip = 7°) thrust event, plausibly on the décollement.

The Kilauea south flank displacement is clearly related to rifting as well as to gravitational load from the mountain edifice, but the temporal relationships between magmatic activity and faulting are complex (e.g., Delaney et al., 1998; Walter & Amelung, 2006). There has been time-varying deformation of the flank over many decades, including décollement slow slip events southwest of the 2018 rupture (e.g., Brooks et al., 2006, 2008; Owen et al., 2000; Segall et al., 2006), again with complex temporal relationship between magmatic activity and earthquake faulting.

The 4 May 2018 earthquake is distinct from the 1975 and 1989 events in that it occurred during a major volcanic sequence, after East Rift Zone fissure eruptions initiated, although the majority of rifting occurred after the event. We determine the rupture characteristics of this important event by analysis of seismic and geodetic observations.

2. Data

We select 26 *P* and 22 *SH* waveforms recorded by global broadband seismic stations with high signal-to-noise ratios and relatively uniform azimuthal distribution in the epicentral distance range 30° to 90° (Figure 2). The instrument responses were deconvolved from the original waveforms to obtain ground velocities (Wald et al., 1996), which are then band-pass filtered between 0.0033 and 1.0 Hz.

We process strong-motion records from 11 stations at epicentral distances less than 100 km (Figure 2). The strong-motion waveform instability at low frequency is removed by applying the correction algorithm of Wang et al. (2011), and the signals are integrated to ground velocity for the frequency band of 0.02 to 0.5 Hz. The processed strong-motion records are aligned on the first *P* arrivals for inclusion in the joint inversion. In addition, coseismic Global Positioning System (GPS) static displacements at 51 sites (Figure 2) from 5-min position time series from continuously operating stations analyzed using GIPSY-OASIS-II software by the University of Nevada Reno (http://geodesy.unr.edu/) are incorporated in the joint inversion. The displacement vectors converge in azimuth, suggesting that slip is concentrated within the along-coast range of the stations. However, the GPS data provide limited resolution of the northeasternmost extent of the 2018 rupture. The strong-motion and GPS station distributions are all on one side of the rupture zone, but provide quite good sensitivity to the source process, although with diminishing resolution seaward.

3. Model Parameterization and Inversion Strategy

An initial rupture model is parameterized with 24 subfaults along strike and 12 along dip on a single planar fault with dimensions of 72 km ×

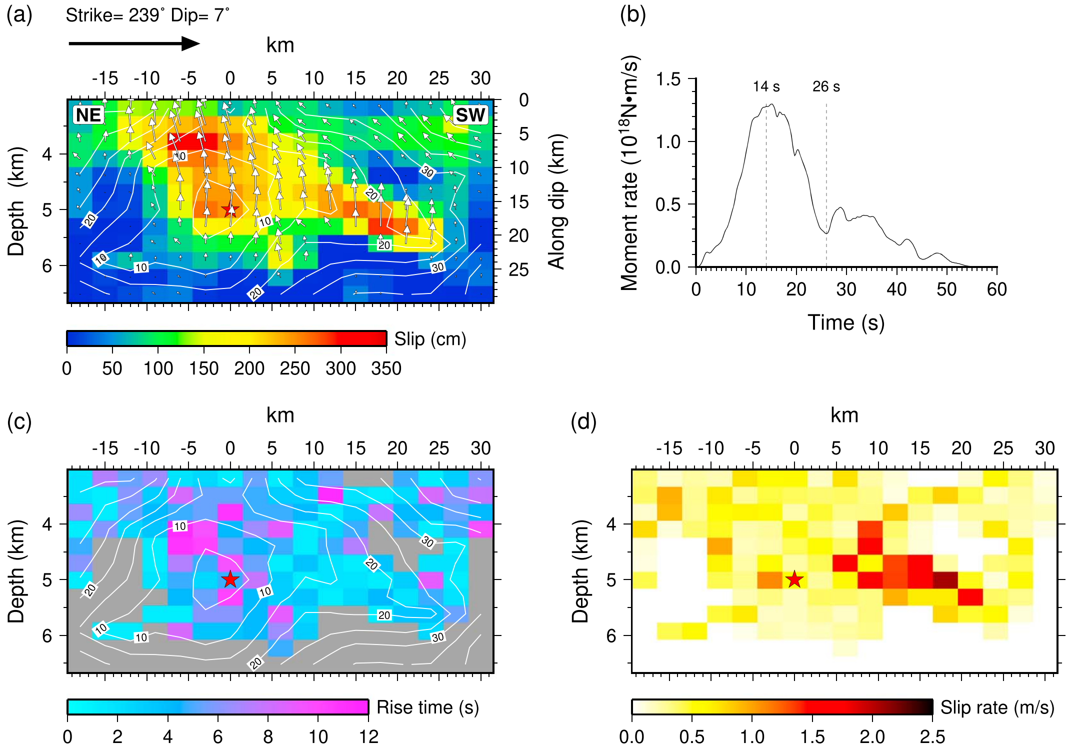

Figure 3. Summary of the preferred finite-fault inversion results. (a) The inverted slip distribution of the 4 May 2018 Hawaii earthquake on the fault model with strike 239° and dip 7°. The red star locates the hypocenter. White contours indicate the rupture initiation time in seconds. White arrows show the variable direction of motion for the hanging wall relative to the footwall in the source reference frame. The color bar shows the slip amplitude scale. (b) The moment rate function for the rupture model. (c) and (d) are the distribution of rise time and slip rate of the rupture model, respectively; subfaults with slip magnitude less than 0.3 m are truncated. Slip rate is defined as the ratio of fault slip and rise time.

30 km. The area of each subfault is 3 km × 2.5 km. For both seismic waves and geodetic statics, we use a 1-D layered velocity model from CRUST2.0 (Bassin et al., 2000). The Green's functions for the teleseismic waves are computed using the reflectivity method and ray theory. The strong-motion Green's functions are generated by applying a frequency-wave number integration algorithm (Zhu & Rivera, 2002), and the Green's functions for the coseismic GPS displacements are calculated by using a generalized reflection-transmission coefficient matrix method developed by Xie and Yao (1989). The strike angle of the fault plane is specified as 239°, in close agreement with the best double-couple solution from the USGS *W*-phase moment tensor solution. We conduct a series of kinematic inversions for the initial rupture model using the strong-motion data and coseismic GPS displacements to search for an optimal hypocentral depth assuming the USGS epicenter (19.313°N, 154.998°W). A hypocentral depth of 5 km produces the best inversion data fit.

The planar fault dip angle is treated as a parameter, given the expected poor resolution for the long-period moment tensor solutions. We performed joint inversions for dips ranging from 3° to 19°, finding good overall waveform fits for dips less than 12° and a best fit for a dip of 7° (Figure S1 in the supporting information). The average dip of the décollement is imaged as about 2° to 5° in offshore reflection images (e.g., Morgan et al., 2000, 2003; Park et al., 2007). The modeling performed here assumes a layered half-space with a horizontal free surface, so the dip estimate is likely affected by dip of the solid rock surface on the flank of the volcano, which is ~3° to 4° in the source region. Thus, a dip of 7° in half-space modeling combined with the 5-km hypocentral depth offshore is likely compatible with the fault being along the décollement. It is also possible that the actual dip does exceed that of the décollement and that some or all of the slip extends onto a steeper dipping splay fault like those imaged beneath the offshore bench (e.g., Morgan et al., 2003). A full three-dimensional calculation for all of the Green's functions would be required to address this further, but that is beyond the scope of this study.

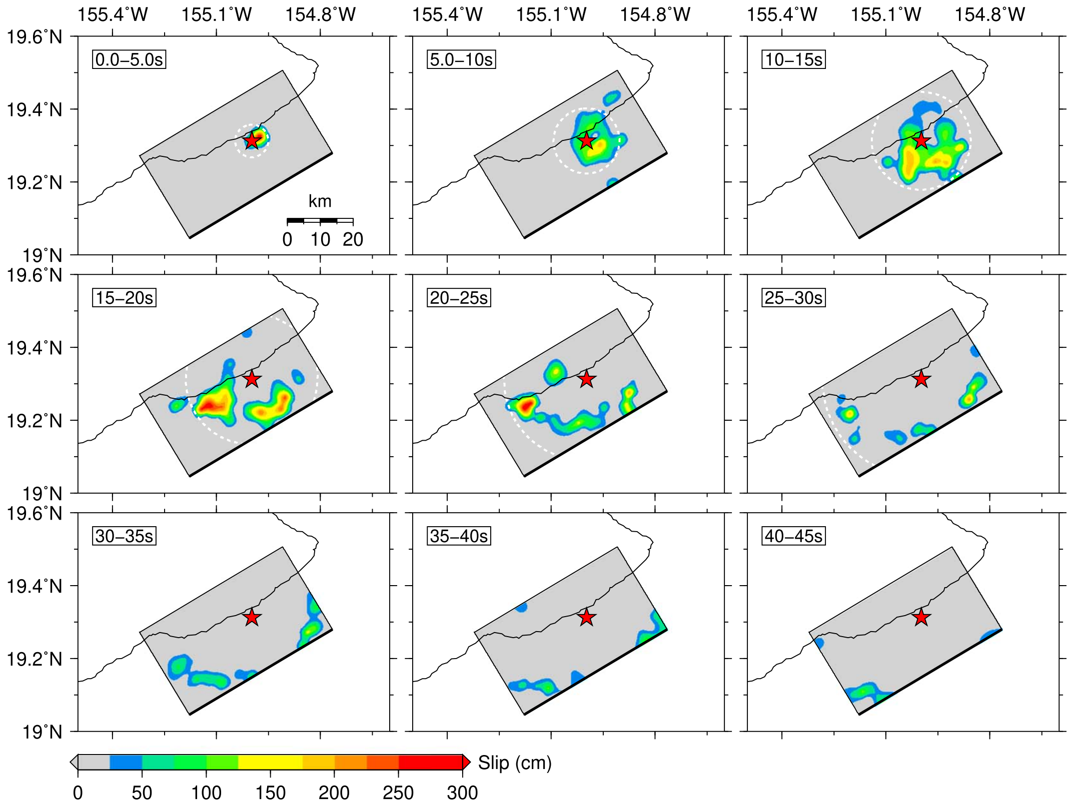

Figure 4. Snapshots of the rupture expansion history during the 4 May 2018 Hawaii earthquake. Colors indicate the fault slip in the indicated time periods. The white dashed contour denotes the pseudo-rupture front with a rupture velocity of 1.0 km/s. the minor slip after 30 s is not considered to be reliably resolved.

For our kinematic source models, we use the finite-fault inversion scheme proposed by Ji et al. (2002), which performs the waveform inversion in the wavelet domain with a simulated annealing method to simultaneously determine slip amplitude, rise time, rake angle, and average rupture velocity. This method allows for joint inversion of coseismic static displacements and seismic waveforms (Liu et al., 2016, 2017; Wei et al., 2012; Yano et al., 2014). Teleseismic *SH* waveforms have half the weight of *P* waveforms, and the various data types are equally weighted in the final inversions. Geodetic observations constrain the total coseismic spatial distribution (Wald & Heaton, 1994), while the seismic wave data sets provide good constraints on the spatiotemporal slip distribution, so these two types of data are complementary. Moreover, two additional constraints are used: (1) the slip differences between neighboring subfaults are minimized and (2) the total seismic moment is constrained to within ±10% of the best double-couple moment from an initial USGS *W*-phase solution (2.79×10^{19} Nm), recognizing that this moment is for a dip of 20°. The error function minimized in the joint inversion is a weighted combination of the seismic waveform misfit in the wavelet domain, the geodetic weighted sum of squared residuals, and space and time smoothing regularizations. During the inversion, the slip amplitude of each subfault varies from 0 to 6 m at 0.2-m intervals and the rake angle varies from 84° to 144° with an interval of 3°. The rise time is allowed to change from 1.2 to 12 s with an increment of 1.2 s. Generally, one of the most influential parameters in kinematic rupture inversions is the rupture velocity. To select this parameter, we conducted a series of seismic inversions with different constant rupture velocities. The average rupture speed is estimated to be somewhere between 0.7 and 1.6 km/s (Figure S2), so the rupture velocity is bounded between 0.5 and 2.0 km/s in the joint inversion. These are relatively low rupture expansion velocities, as also found in the USGS finite-fault model (https://earthquake.usgs.gov/earthquakes/eventpage/us1000dyad#finite-fault), which may be associated with rupture on the weak surface of the Pacific plate.

Checkerboard inversions of the combined data sets using the initial fault that extends northeast of the eastern tip of Hawaii confirms that our data provide limited resolution of slip in the northeast region and in the shallowest portion of the fault model, offshore (Figure S3). We therefore adopt a shorter final rupture model with 17 subfaults along strike extending to near Kapoho; the entire fault dimension is 51 km × 30 km.

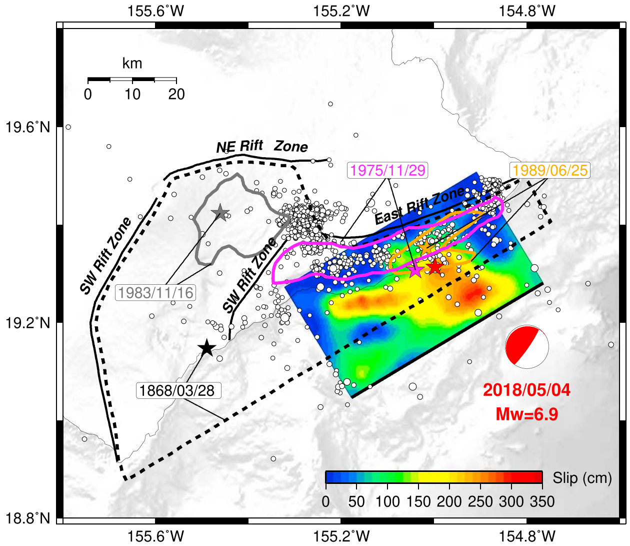

Figure 5. Map view of the surface projection of the 4 May 2018 Hawaii earthquake slip distribution along with rupture areas of large historical earthquakes. The 2018 earthquake epicenter is shown with a red star. The red focal mechanism indicates the faulting geometry, with a 7° dipping plane plunging northwestward. White dots show the first month of aftershocks of the 2018 event for $M \geq 2.5$. The black star and dotted line are the epicenter and proposed rupture area of the great 1868 Kau earthquake (Wyss, 1988). The purple, gray, and orange stars and lines are the epicenters and estimated rupture areas of the 1975, 1983, and 1989 events, respectively, inferred from aftershock zones, flank geometry, and seismicity (Klein et al., 2001). These likely underestimate extent of offshore slip for the 1989 and 1975 events judging from the sparse offshore seismicity for the 2018 event. The thick black lines indicate active rift zones.

4. Results

The preferred final slip distribution, moment rate function, rise time, and slip rate are shown in Figure 3. A region with large slip locates offshore beneath the submarine flank of Kilauea volcano, spanning ~50 km along strike and ~25 km along dip (Figure 3a). The total allowed rupture duration is 45 s, but the resolved seismic energy release is within the first ~ 30 s (Figure 3b). This is compatible with the GCMT centroid duration of 14.7 s. The initial onset of the moment rate function with very low slip is not well resolved. The subfault rise time estimates have a complex pattern (Figure 3c), but the region of large shallow slip has relatively long rise times of 6–12 s. The checkerboard tests indicate reasonable resolution of the large slip patches but increased uncertainty for shallow slip. The slip rate is defined as the ratio of fault slip to rise time. Large slip rates are found in the southwestern slip patch near the coast. The mean average rise time and slip rate are 4.3 s and 0.5 m/s, respectively. The seismic moment of our preferred model is 2.5×10^{19} Nm, which gives $M_W = 6.86$. The peak slip amplitudes in the model are located southwest and updip of the hypocenter. The centroid depth of the slip distribution is ~5 km, which is shallower than the GCMT centroid (12 km) but generally consistent with the offshore décollement geometry. Comparisons between observations and predictions for all data sets are shown in Figures S4 to S6. The preferred rupture model predicts the main features of the GPS horizontal and vertical static offsets (Figure S4), particularly the convergence of the horizontal displacements. The longer-period arrivals in the strong-motion observations are fit well (Figure S5) other than for a few signals, notably station 2836. Station 2836 is located near the Kilauea volcano summit, so the relatively large misfit can be partially attributed to unmodeled complex velocity structure (Figures S7 and S8 show an inversion using more heavily filtered strong-motion signals). The teleseismic body wave observations are fit well other than for initial cycles on some of the *P* waves (Figure S6).

Figure 4 shows snapshots of the rupture expansion in the preferred model, revealing a complex source process. Initially, the rupture nucleates near the hypocenter and then expands northward during the first 5 s. The main slip patch slowly spreads radially (<1 km/s) after 5 s and then propagates updip and along strike toward the southwest with a higher slip rate from 15 to 25 s (Figure 3d). Peak slip values are around 3.0 m. The seismic moment rate peaks around 15 s, then begins to tail off (Figure 3b). The resolved rupture is complete by ~30 s, and we do not have confidence in weak features in the moment rate function or in the slip model beyond that time, as both originate in the shallow updip part of the model which has poor resolution.

5. Discussion and Conclusions

The 4 May 2018 M_W 6.9 earthquake is the largest to strike the Kilauea volcano East Rift Zone since the 1975 Kalapana M_W 7.7 earthquake. The preferred slip model is shown in map view in Figure 5. The rupture occurred on a shallowly dipping plane plunging toward the island center, with the main slip located seaward of the coast around 5 km deep. Aftershocks tend to fringe the areas of large slip and are not particularly abundant in the offshore portion of the fault. This suggests that inferences of the slip region of prior events based on aftershock distributions, as shown in Figure 5, may be unreliable in this region. The model parameters indicate that the event plausibly ruptured the décollement between the island mass and the former Pacific seafloor.

The slip is concentrated offshore, and we find similar slip distributions and fits to the data for models with a 4° dip (Figures S8 to S12) and a 10° dip (Figures S13 to S16), so the offshore slip placement is relatively robustly resolved by the data. We lack resolution of the northeastern extent of slip, but we note that there is relatively little early aftershock seismicity beyond the extent of our preferred model, and major rifting in the northeast near Kapoho did not commence until several weeks after the 4 May earthquake. The rupture zone may overlap the slip zones of the 1975 and 1989 events (Figure 5), although slip distributions for those events are not well constrained.

The 1975 event clearly ruptured offshore similar to the 2018 event, as both generated tsunami. Recorded tsunami amplitudes of less than 30 cm in Hilo are compatible with our model. Tsunami recordings for the 1975 event were much larger (e.g., Ma et al., 1999). The rupture duration (~30 s) is relatively long for an M_W 6.9 thrust event (e.g., Ye et al., 2016). For example, the M_W 6.9 Loma Prieta, California earthquake has an ~8-s duration. The broadband radiated seismic energy computed by IRIS for the event is $E_R = 8.9 \times 10^{13}$ J (https://doi.org/10.17611/DP/EQE.1; Convers & Newman, 2011). The moment-scaled radiated energy $E_R/M_0 = 3.6 \times 10^{-6}$, using the *W*-phase seismic moment, is very low relative to typical interplate thrust events and is comparable to those for tsunami earthquakes (e.g., Newman & Okal, 1998; Ye et al., 2016). The low rupture velocity, long duration, and low moment-scaled radiated energy indicate frictional properties similar to those in the shallow portion of subduction zones where tsunami earthquakes occur. This is likely the result of abyssal sediments on the Pacific plate influencing the friction along the décollement.

The 2018 event occurred after initiation of rifting in the Leilani Estates, so it is tempting to infer that it was directly driven by the rifting. However, while the event may have been triggered by the dike injection or by stress waves from a magnitude 5.4 thrust-faulting earthquake that occurred a few kilometers to the northwest and 1 hr before the 6.9, the main slip likely reflects release of strain accumulated since the 1975 and 1989 events associated with progressive southwestward deformation of the mobile south flank of Kilauea, which is frictionally resisted by coupling of the décollement. This region of strain accumulation and faulting in 2018 lies northeast of the region of slow slip events during the past few decades. The primary rift volcanism in the 2018 eruption, with extrusions exceeding 500,000,000 m^3 at the time of writing, largely occurred after the rupture, so the earthquake may have had more direct influence on the rifting than vice versa. Comparable cumulative eruptions of material in the East Rift Zone in 1955 to 1960 did not produce a large synchronous décollement earthquake. Nevertheless, the processes are clearly linked and the 2018 earthquake can be viewed as an integral part of the 2018 volcanic process in Kilauea, although the temporal relationship is distinct from that for the 1975 and 1989 events (which were not accompanied by synchronous East Rift Zone magmatism). So, the physical interaction between compressional strains from dike injection and extensional strains from décollement thrusting remains poorly understood (e.g., Delaney et al., 1998).

Laboratory experiments (e.g., Noda et al., 2013) suggest that earthquake faulting begins with accelerating aseismic rupture growth over a nucleation zone. Thus, large earthquakes may start by a nucleation process, which could be manifested in a cascade of migrating foreshocks. Several large subduction earthquakes were preceded by precursory migrating seismic sequences, such as the 2011 Tohoku-Oki earthquake (e.g., Kato et al., 2012) and the 2014 Iquique earthquake (e.g., Ruiz et al., 2014). Seismicity in the few days prior to the 2018 Hawaii event was primarily localized along the East Rift zone, but a southeastward trending sequence did migrate over several days to near the mainshock epicenter (Figure S17). The largest of these events was a M_W 5.4 thrust event. Plausibly, the mainshock initiation area was a relatively strong patch with high fracture energy, and the rupture was dynamically triggered by the migrating sequence of small foreshocks.

Acknowledgments
Teleseismic body wave recordings were downloaded from the Incorporated Research Institutions for Seismology (IRIS) data management center (http://ds.iris.edu/wilber3/find_event). Strong-motion recording were obtained from the USGS National Strong-Motion Project (NSMP; https://earthquake.usgs.gov/monitoring/nsmp/). GPS displacements were obtained from the Nevada Geodetic Laboratory (NGL, http://geodesy.unr.edu/), which obtained the raw GPS data from continuously operating GPS stations operated by the USGS Hawaiian Volcano Observatory, University of Hawaii, Stanford University, the Jet Propulsion Lab, U.S. Coast Guard, and Federal Aviation Authority. We thank Chao An in School of Naval Architecture, Ocean and Civil Engineering, Shanghai Jiao Tong University for useful suggestions and helpful discussion. Two anonymous reviewers gave constructive suggestions on the manuscript. T. Lay's research on earthquakes is supported by the U.S. National Science Foundation grant EAR1802364. This work is also supported by National Science Foundation of China (grants 41731072 and 41604057).

References

Ando, M. (1979). The Hawaii earthquake of November 29, 1975: Low dip angle faulting due to forceful injection of magma. *Journal of Geophysical Research*, *84*(B13), 7616–7626. https://doi.org/10.1029/JB084iB13p07616

Bassin, C., Laske, G., & Masters, G. (2000). The current limits of resolution for surface wave tomography in North America. *Eos, Transactions American Geophysical Union*, *81*, F897.

Brooks, B. A., Foster, J., Sandwell, D., Wolfe, C. J., Okubo, P., Poland, M., & Myer, D. (2008). Magmatically triggered slow slip at Kilauea volcano, Hawaii. *Science*, *321*(5893), 1177. https://doi.org/10.1126/science.1159007

Brooks, B. A., Foster, J. H., Bevis, M., Frazier, L. N., Wolfe, C. J., & Behn, M. (2006). Periodic slow earthquakes on the flank of Kilauea volcano, Hawaii. *Earth and Planetary Science Letters*, *246*(3-4), 207–216. https://doi.org/10.1016/j.epsl.2006.03.035

Broyles, M. L., Suyenaga, W., & Furumoto, A. S. (1979). Structure of the lower east rift zone of Kilauea volcano, Hawaii, from seismic and gravity data. *Journal of Volcanology and Geothermal Research*, *5*(3-4), 317–336. https://doi.org/10.1016/0377-0273(79)90022-2

Convers, J. A., & Newman, A. V. (2011). Global evaluation of large earthquake energy from 1997 through mid-2010. *Journal of Geophysical Research*, *116*, B08304. https://doi.org/10.1029/2010JB007928

Crosson, R. S., & Endo, E. T. (1982). Focal mechanisms and locations of earthquakes in the vicinity of the 1975 Kalapana earthquake aftershock zone 1970–1979: Implications for tectonics of the south flank of Kilauea volcano, island of Hawaii. *Tectonics*, *1*(6), 495–542. https://doi.org/10.1029/TC001i006p00495

Day, S. J., Watts, P., Grilli, S. T., & Kirby, J. T. (2005). Mechanical models of the 1975 Kalapana, Hawaii earthquake and tsunami. *Marine Geology*, *215*(1-2), 59–92. https://doi.org/10.1016/j.margeo.2004.11.008

Delaney, P. T., Denlinger, R. P., Lisowski, M., Miklius, A., Okubo, P. G., Okamura, A. T., & Sako, M. K. (1998). Volcanic spreading at Kilauea, 1976–1996. *Journal of Geophysical Research*, *103*(B8), 18,003–18,023. https://doi.org/10.1029/98JB01665

Denlinger, R. P., & Okubo, P. (1995). Structure of the mobile south flank of Kilauea volcano, Hawaii. *Journal of Geophysical Research*, *100*(B12), 24,499–24,507. https://doi.org/10.1029/95JB01479

Eissler, H. K., & Kanamori, H. (1987). A single-force model for the 1975 Kalapana, Hawaii, earthquake. *Journal of Geophysical Research*, *92*(B6), 4827–4836. https://doi.org/10.1029/JB092iB06p04827

Ekström, G., Nettles, M., & Dziewonski, A. M. (2012). The global CMT project 2004–2010: Centroid-moment tensors for 13,017 earthquakes. *Physics of the Earth and Planetary Interiors*, *200-201*, 1–9. https://doi.org/10.1016/j.pepi.2012.04.002

Furumoto, A. S., & Kovach, R. L. (1979). The Kalapana earthquake of November 29, 1975: An intra-plate earthquake and its relation to geothermal processes. *Physics of the Earth and Planetary Interiors*, *18*(3), 197–208. https://doi.org/10.1016/0031-9201(79)90114-6

Gillard, D., Wyss, M., & Okubo, P. (1996). Type of faulting and orientation of stress and strain as a function of space and time in Kilauea's south flank, Hawaii. *Journal of Geophysical Research*, *101*(B7), 16,025–16,042. https://doi.org/10.1029/96JB00651

Ji, C., Wald, D. J., & Helmberger, D. V. (2002). Source description of the 1999 Hector Mine, California, earthquake, Part I: Wavelet domain inversion theory and resolution analysis. *Bulletin of the Seismological Society of America*, *92*(4), 1192–1207. https://doi.org/10.1785/0120000916

Kato, A., Obara, K., Igarashi, T., Tsuruoka, H., Nakagawa, S., & Hirata, N. (2012). Propagation of slow slip leading up to the 2011 M_W 9.0 Tohoku-Oki earthquake. *Science*, *335*(6069), 705–708. https://doi.org/10.1126/science.1215141

Kawakatsu, H. (1989). Centroid single force inversion of seismic waves generated by landslides. *Journal of Geophysical Research*, *94*(B9), 12,363–12,374. https://doi.org/10.1029/JB094iB09p12363

Klein, F. W., Frankel, A. D., Mueller, C. S., Wesson, R. L., & Okubo, P. G. (2001). Seismic hazard in Hawaii: High rate of large earthquakes and probabilistic ground-motion maps. *Bulletin of the Seismological Society of America*, *91*(3), 479–498. https://doi.org/10.1785/0120000060

Liu, C., Zheng, Y., Wang, R., Shan, B., Xie, Z., Xiong, X., & Ge, C. (2016). Rupture processes of the 2015 M_W 7.9 Gorkha earthquake and its M_W 7.3 aftershock and their implications on the seismic risk. *Tectonophysics*, *682*, 264–277. https://doi.org/10.1016/j.tecto.2016.05.034

Liu, C., Zheng, Y., Xie, Z., & Xiong, X. (2017). Rupture features of the 2016 M_W 6.2 Norcia earthquake and its possible relationship with strong seismic hazards. *Geophysical Research Letters*, *44*, 1320–1328. https://doi.org/10.1002/2016GL071958

Ma, K.-F., Kanamori, H., & Satake, K. (1999). Mechanism of the 1975 Kalapana, Hawaii, earthquake inferred from tsunami data. *Journal of Geophysical Research*, *104*, 13,153–13,167.

Morgan, J. K., Moore, G. F., & Clague, D. A. (2003). Slope failure and volcanic spreading along the submarine south flank of Kilauea volcano, Hawaii. *Journal of Geophysical Research*, *108*(B9), 2415. https://doi.org/10.1029/2003JB002411

Morgan, J. K., Moore, G. F., Hills, D. J., & Leslie, S. (2000). Overthrusting and sediment accretion along Kilauea's mobile south flank, Hawaii: Evidence for volcanic spreading from marine seismic reflection data. *Geology*, *28*(7), 667–700. https://doi.org/10.1130/0091-7613(2000)28<667:OASAAK>2.0.CO;2

Nettles, M., & Ekström, G. (2004). Long-period source characteristics of the 1975 Kalapana, Hawaii, earthquake. *Bulletin of the Seismological Society of America*, *94*(2), 422–429. https://doi.org/10.1785/0120030090

Newman, A. V., & Okal, E. A. (1998). Teleseismic estimates of radiated seismic energy: The E/M_0 discriminant for tsunami earthquakes. *Journal of Geophysical Research*, *103*(B11), 26,885–26,898. https://doi.org/10.1029/98JB02236

Noda, H., Nakatani, M., & Hori, T. (2013). Large nucleation before large earthquakes is sometimes skipped due to cascade-up—Implications from a rate and state simulation of faults with hierarchical asperities. *Journal of Geophysical Research: Solid Earth*, *118*, 2924–2952. https://doi.org/10.1002/jgrb.50211

Owen, S., Segall, P., Lisowski, M., Miklius, A., Denlinger, R., & Sako, M. (2000). Rapid deformation of Kilauea volcano: Global Positioning System measurement between 1990 and 1996. *Journal of Geophysical Research*, *105*(B8), 18,983–18,998. https://doi.org/10.1029/2000JB900109

Park, J., Morgan, J. K., Zelt, C. A., Okubo, P. G., Peters, L., & Benesh, N. (2007). Comparative velocity structure of active Hawaiian volcanoes from 3-D onshore-offshore seismic tomography. *Earth and Planetary Science Letters*, *259*(3-4), 500–516. https://doi.org/10.1016/j.epsl.2007.05.008

Ruiz, S., Metois, M., Fuenzalida, A., Ruiz, J., Leyton, F., Grandin, R., et al. (2014). Intense foreshocks and a slow slip event preceded the 2014 Iquique *Mw* 8.1 earthquake. *Science*, *345*(6201), 1165–1169. https://doi.org/10.1126/science.1256074

Segall, P., Desmarais, E. K., Shelly, D., Miklius, A., & Cervelli, P. (2006). Earthquakes triggered by silent slip events on Kilauea volcano, Hawaii. *Nature*, *442*(7098), 71–74. https://doi.org/10.1038/nature04938

Swanson, D. A., Duffield, W. A., & Fiske, R. S. (1976). Displacement of the south flank of Kilauea volcano: The result of forceful intrusion of magma into the rift zones. *Geological Survey Professional Paper*, *963*, 44.

Thurber, C. H., & Gripp, A. E. (1988). Flexure and seismicity beneath the south flank of Kilauea volcano and tectonic implications. *Journal of Geophysical Research*, *93*(B5), 4271–4278. https://doi.org/10.1029/JB093iB05p04271

Wald, D. J., & Heaton, T. H. (1994). Spatial and temporal distribution of slip for the 1992 Landers, California, earthquake. *Bulletin of the Seismological Society of America*, *84*(3), 668–691.

Wald, D. J., Heaton, T. H., & Hudnut, K. W. (1996). The slip history of the 1994 Northridge, California, earthquake determined from strong-motion, teleseismic, GPS, and leveling data. *Bulletin of the Seismological Society of America*, *86*, S49–S70.

Walter, T. R., & Amelung, F. (2006). Volcano-earthquake interaction at Mauna Loa volcano, Hawaii. *Journal of Geophysical Research*, *111*, B05204. https://doi.org/10.1029/2005JB003861

Wang, R., Schurr, B., Milkereit, C., Shao, Z., & Jin, M. (2011). An improved automatic scheme for empirical baseline correction of digital strong-motion records. *Bulletin of the Seismological Society of America*, *101*(5), 2029–2044. https://doi.org/10.1785/0120110039

Wei, S., Graves, R., Helmberger, D., Avouac, J. P., & Jiang, J. (2012). Sources of shaking and flooding during the Tohoku-Oki earthquake: A mixture of rupture styles. *Earth and Planetary Science Letters*, *333*, 91–100.

Wyss, M. (1988). A proposed source model for the great Kau, Hawaii, earthquake of 1868. *Bulletin of the Seismological Society of America*, *78*(4), 1450–1462.

Wyss, M., & Kovach, R. L. (1988). Comment on "A single-force model for the 1975 Kalapana, Hawaii earthquake" by Holly K. Eissler and Hiroo Kanamori. *Journal of Geophysical Research*, *93*(B7), 8078–8082. https://doi.org/10.1029/JB093iB07p08078

Xie, X., & Yao, Z. (1989). A generalized reflection-transmission coefficient matrix method to calculate static displacement field of a dislocation source in a stratified half space. *Chinese Journal of Geophysics*, *32*, 191–205.

Yano, T. E., Shao, G., Liu, Q., Ji, C., & Archuleta, R. J. (2014). Coseismic and potential early afterslip distribution of the 2009 M_W 6.3 L'Aquila, Italy earthquake. *Geophysical Journal International*, *199*(1), 23–40. https://doi.org/10.1093/gji/ggu241

Ye, L., Lay, T., Kanamori, H., & Rivera, L. (2016). Rupture characteristics of major and great ($M_W \geq 7.0$) megathrust earthquakes from 1990 to 2015: 1. Source parameter scaling relationships. *Journal of Geophysical Research: Solid Earth*, *121*, 826–844. https://doi.org/10.1002/2015JB012426

Zhu, L., & Rivera, L. A. (2002). A note on the dynamic and static displacements from a point source in multilayered media. *Geophysical Journal International*, *148*(3), 619–627. https://doi.org/10.1046/j.1365-246X.2002.01610.x